Supplementary Information

In-situ Hydrogen Production in All-Level-Humidity Air: Integrating Atmospheric Water Harvesting with Photocatalysis

Xueli Yan[a], Li Tian[a], Fei Xue[a], Jie Huang[a], Rui Zhao[a], Xiangjiu Guan[a,*], Jinwen Shi[a,*], Wenshuai Chen[c,*], Maochang Liu [a,b,*]

[a]*International Research Center for Renewable Energy & State Key Laboratory of Multiphase Flow in Power Engineering, Xi'an Jiaotong University, Xi'an 710049, P. R. China*

[b]*Suzhou Academy of Xi'an Jiaotong University, Suzhou 215123, P. R. China*

[c]*Key Laboratory of Bio-based Material Science and Technology, Ministry of Education, Northeast Forestry University, Harbin 150040, P. R. China*

**To whom correspondence should be addressed. Email: xj-guan@mail.xjtu.edu.cn (X. Guan), jinwen_shi@mail.xjtu.edu.cn (J. Shi), chenwenshuai@nefu.edu.cn (W. Chen), maochangliu@mail.xjtu.edu.cn (M. Liu).*

Table of Contents

S1. Experimental section

S1.1. Resource availability

S1.2. Synthesis of $SrTiO_3$:Al

S1.3. Synthesis of NFC suspensions

S1.4. Synthesis of NFC@LiCl-$SrTiO_3$:Al

S1.5. Design of device for photocatalytic water splitting for H_2 production

S1.6. Material characterization

S1.7. Atmospheric water uptake

S1.8. Photocatalytic reactions

S.1.9. Practical outdoor in-situ H_2 production from air

S1.10. Electronic energy band structure test of $SrTiO_3$:Al

S1.11. Detection of $\cdot O_2^-$

S1.12. Detection of H_2O_2

S2. Supporting Tables

S3. Supporting Figures

S4. Supporting References

S1. Experimental section

S1.1. Resource availability

Lead contact

Further information and requests for resources and reagents should be directed to and will be fulfilled by the lead contact, Maochang Liu (maochangliu@mail.xjtu.edu.cn).

Materials availability

All reagents were analytical grade and used without further purification. Sodium chlorite ($NaClO_2$), acetic acid ($C_2H_4O_2$, 98%), potassium hydroxide (KOH), strontium chloride hexahydrate ($SrCl_2·6H_2O$), aluminum oxide (Al_2O_3), strontium titanate ($SrTiO_3$), sodium hexachlororhodate (Na_3RhCl_6), potassium chromate (K_2CrO_4), lithium chloride (LiCl), sodium sulfate (Na_2SO_4), potassium hydrogen phthalate ($C_8H_5KO_4$), potassium iodide (KI), hydrogen peroxide (H_2O_2), and 5-dimethyl-1-pyrrolidine-N-oxide (DMPO) were purchased from Sinopharm Chemical Reagen Co., Ltd. Ultrahigh purity argon (Ar, ≥99.999%) was provided by Shanxi Xinkang Medical Oxygen Co., Ltd. The poplar wood was supplied by pet store. The water used throughout the experiments are de-ionized water with a resistivity of 18.2 MΩ cm.

Data and code availability

The data that support the plots of this study may be reasonably requested from the corresponding authors.

S1.2. Synthesis of $SrTiO_3$:Al

The $SrTiO_3$:Al was fabricated according to our previous reported methods.[1] Specifically, the mixture of $SrTiO_3$, $SrCl_2·6H_2O$, and Al_2O_3 were mixed homogeneously *via* grinding in a molar ratio of 1:10:0.02, calcined in an alumina crucible in air at 1100°C for 5 h. After being cooled to room temperature, the obtained powders were washed 5 times with water and dried at 60°C in air for 10 h.

The Rh/CrO_x co-catalysts were loaded into $SrTiO_3$:Al via photo-deposition method. Briefly, it was prepared by adding $SrTiO_3$:Al (100 mg) to the mixture solution of H_2O (64 mL) and methanol (16 mL) with Na_3RhCl_6 (corresponding to a loading amount of 0.6wt% Rh on $SrTiO_3$:Al) dispersed homogeneously by ultrasonication. Afterwards, the mixed solution was transferred to a Pyrex glass photocatalytic reactor with a volume of 105 mL with a circulating

water jacket and bubbled for 15 min using Ar to exhaust the air before irradiation with a 300 W Xe lamp (Perfect Light PLS-SXE300+, China) for 1 h. Afterwards, K_2CrO_4 (corresponding to a loading amount of 1.0wt% Cr on $SrTiO_3$:Al) was added to the solution and irradiated for another 1 h. The reaction was carried out through continuous stirring using a magnetic stirrer and the reaction temperature was maintained at 35°C using circulating water. After the reaction, the reaction solution was centrifuged, washed three times with deionized water, and dried at 60°C in air overnight.

S1.3. Synthesis of NFC suspensions

Nanofibrillar cellulose (NFC) suspensions were prepared by purification of poplar wood powder following the well-reported chemical treatment coupled with mechanical methods with a slight modification.[2, 3] Typically, it was prepared by adding $NaClO_2$ (4 g) to aqueous solution (400 g), followed by drops of acetic acid to tune the pH of the reaction solution (pH=4.7) to obtain an aqueous solution of acidified $NaClO_2$. The entire process was carried out under magnetic stirring. Subsequently, poplar wood powder (10 g) was dissolved to the above solution in a 500 mL single-necked flask and reacted at 75°C for 1 h in a preheated oil bath. This procedure was repeated 5 times to remove a number of lignin from the wood powder. Afterwards, the reactants were reacted in 400 g of aqueous KOH (5 wt%) in a preheated oil bath at 90°C for 2 h to remove a set of hemicellulose. The sample was further treated with acidified $NaClO_2$ solution at 75°C for 1 h (2 times) and with 5 wt% KOH solution at 90°C for 2 h. Each procedure was followed by filtration and washing with deionized water to obtain chemically purified cellulose pulp. Finally, the as-prepared undried cellulose pulp was suspended in deionized water and nano-fibrillated using an ultrasonic crusher (Saifei Biosafer 3D, China) for 60 min to generate a 1 wt% NFC suspension.

S1.4. Synthesis of NFC@LiCl-$SrTiO_3$:Al

NFC@LiCl-$SrTiO_3$:Al (NLS) was fabricated via a combination of solution replacement and freeze-drying methods. Initially, 30 g of NFC suspension (1 wt%) was placed in a 150 mL freezing mold. Subsequently, 3 mL of $SrTiO_3$:Al (20 mg) aqueous solution was uniformly dispersed on the surface of NFC suspension. The samples were allowed to stand at room temperature for 12 h to generate a $SrTiO_3$:Al/NFC composite gel. Afterwards, 50 g of LiCl

aqueous solution (5 wt%) was slowly dripped into the above sample along the inner wall of the mold, followed by removal of the excess LiCl solution after 24-h resting time at room temperature. Finally, the gel in the freezing mold was pre-cooled in a -30°C refrigerator and immediately freeze-dried for 48 h to synthesize NLS-20. For the preparation of NLS series, the procedures were kept the same except that different amounts of $SrTiO_3$:Al (5 mg, 10 mg, 20 mg, 40 mg, and 80 mg) dispersions were dropped onto the surface of the NFC suspension prior to the solution displacement. The modified NLS was designated as NLS-*x*. Here, *x* = 5, 10, 20, 40, and 80, indicating the amount of $SrTiO_3$:Al used during the synthesis. For the synthesis of NFC@LiCl (NL), the processes were similar to that of NLS, except that the $SrTiO_3$:Al dispersion was not used to drop onto the surface of NFC suspension prior to the solution displacement reaction, as well as being left at room temperature for 12 h.

S1.5. Design of device for photocatalytic water splitting for H_2 production

The novel overhead illumination device for photocatalytic water splitting under atmospheric pressure was designed, in the case of that prepared NLS-*x* is a round block gel with a diameter of about 3.5 cm (Figure S12). The device is composed of a quartz light-transmitting cover attached to reaction chamber, which were sealed by a sealing gasket and three sets of clips. The inlet side of the reaction chamber is connected to Ar through the first vacuum valve, where the outlet side is equipped with the second vacuum valve, and the gas sampling port is provided in the upper part. Specifically, the overhead illumination device for photocatalytic water splitting under atmospheric pressure was sealed after putting the moisture-absorbing NLS in reaction chamber. Prior to the reaction, the reaction chamber was purged with Ar for 3 min through connecting Ar to the first vacuum valve. After the purge, the second vacuum valve was closed, followed by the first vacuum valve. Finally, the Xe lamp light source (Perfect Light PLS-SXE300+, China) was turned on, whose current was tuned for photocatalytic water splitting.

S1.6. Material characterization

N_2 adsorption-desorption isotherms were measured at 77 K using an accelerated surface area and porosimetry analyzer (Micromeritics ASAP 2460, USA). Specific surface areas of samples were determined based on the Brunauer-Emmett-Teller (BET) approach, and pore-size distributions and pore volumes of samples were estimated based on Barrett-Joyner-Halenda

(BJH) approach. Scanning electron microscopy (SEM) images of the prepared samples were observed by a field-emission scanning electron microscope (JEOL JSM-7800F, Japan). Transmission electron microscopy (TEM) images of samples were collected using a microscope (FEI Tecnai G^2 F30 S-Twin, USA) attached with a detector (OXFORD MAX-80, UK) for collecting energy-dispersive X-ray spectroscopy (EDX) signals at 300 kV. Powder X-ray diffraction (XRD) patterns were acquired from a diffractometer (PANalytical X'pert MPD Pro, Netherlands) with scan range between 5° and 90° using Cu Kα irradiation (λ =1.5406 Å, 40 kV/40 mA). Fourier-transform infrared (FTIR) spectra were measured by an FTIR spectrophotometer (Bruker Vertex70, Germany) in the wavenumber range of 4000 ~ 500 cm^{-1}. The X-ray photoelectron spectroscopy (XPS) spectra were recorded on a spectrometer (Kratos Axis Ultra DLD, Japan) equipped with a standard and monochromatic Al Kα line as the excitation source (hv = 1486.6 eV), and were calibrated with the adventitious C 1s peak at 284.8 eV. Ultraviolet–visible (UV–vis) spectrum were confirmed by a UV–vis NIR spectrophotometer (Agilent Cary 5000, USA) in the range of 300~800 nm. Steady-state photoluminescence (PL) spectra qualitatively evaluating the recombination of photogenerated carriers were acquired from steady state & lifetime fluorescence spectrometer (Edinburgh Instruments FLS1000, UK) with an excitation wavelength of 365 nm. Curves of thermogravimetric analysis (TGA) were characterized by a thermal analyzer (NETZSCH STA 449 C, Germany) in air atmosphere with the range from 30 to 850°C and a ramp rate of 10°C min^{-1}. The wettability of the sample's surface was characterized by measuring the contact angle (CA) of deionized water on an optical CA measuring instrument (Biolin Theta lite, Finland) in ambient air at room temperature. The infrared images of the samples were taken by a thermal imaging camera (FLIR One Pro, US). Reactive radicals of water oxidation intermediates during photocatalytic reactions were detected by an electron paramagnetic resonance (EPR) instrument (Bruker EMX, Germany) at a microwave frequency of 9.40 GHz.

S1.7. Atmospheric water uptake

The prepared NL as well as NLS-*x* were placed in a constant temperature and humidity chamber (Shanghai Langxuan Experimental Equipment Co., Ltd. SPX-150-C, China) for 24 h to evaluate the atmospheric water uptake capacity of the samples under different humidity

environments. Meanwhile, the mass change of the samples was recorded on an electronic balance (METTLER TOLEDO ME204E, Switzerland) with an accuracy of 0.0001 g. It should be noted that the water absorption test of each material was repeated 3 times. The moisture uptake of the samples during moisture absorption was calculated by Equation (1):

$$\text{Moisture uptake} = \frac{m_i - m_a}{m_a} \quad (1)$$

where m_i denotes the mass of samples after moisture absorption at various times, and m_a is the initial weight of sample before absorption.

S1.8. Photocatalytic reactions

Photocatalytic reactions of H_2 production by atmospheric water splitting were conducted in a 130 mL device designed in Section 1.5 with overhead irradiation at ambient temperature using a Xe lamp irradiation (Perfect Light PLS-SXE300+, China). In detail, the NLS-*x* saturated with moisture in air was placed in device, irradiated by Xe lamp after being evacuated by Ar for 3 min. The evolved gases were analyzed per 1 h by gas chromatography (Bruker GC-450, Germany) equipped with a thermal conductivity detector (TCD) and high-purity Ar as the carrier gas.

The solar-to-H_2 (STH) energy conversion efficiency was evaluated using a 300 W Xe lamp (Perfect Light PLS-SXE300+, China) as simulated solar light source. The light intensity was measured using a photo radiometer (Perfect Light PL-MW 2000, China). The STH was calculated according to Equation (2):

$$\text{STH} = \frac{\text{R}_{\text{H}_2} \times \Delta G_r}{P_{\text{sun}} \times S} \times 100\% \quad (2)$$

where R_{H_2} represents the rate of photocatalytic water splitting for H_2 production (mmol s^{-1}). The R_{H_2} of NLS-20 after moisture absorption in 90% RH and 25% RH environments were 1.82×10^{-5} and 4.45×10^{-6} mmol s^{-1}, respectively. Molar Gibbs free energy of water splitting reaction (J mol^{-1}), P_{sun} is irradiated intensity (1.4904 sun) of NLS-20 under Xe lamp, S is irradiated area (9.62 cm^2). Standard molar Gibbs free energy of water splitting, $\Delta G^{\theta}_{r} = 237$ kJ mol^{-1}.

The STH of NLS-20 after moisture absorption in 90% RH calculated from Equation (2):

$$\mathrm{STH} = \frac{1.82 \times 10^{-5} \times 2.37 \times 10^{-3}}{1.4904 \times 9.62} \times 100\% = 0.3\%$$

The STH of NLS-20 after moisture absorption in 30% RH calculated from Equation (2):

$$\mathrm{STH} = \frac{4.45 \times 10^{-6} \times 2.37 \times 10^{-3}}{1.4904 \times 9.62} \times 100\% = 0.07\%$$

S.1.9. Practical outdoor in-situ H_2 production from air

The outdoor in-situ H_2 production from air experiment utilizing the NLS-20 was conducted on July 24 and 25, 2024, at the Xingqing Campus of Xi'an Jiaotong University. The hygroscopic process was identical to that described in Section S1.7, with the exception that the hygroscopic environment was outdoors. Similarly, the H_2 production process mirrored that of Section S1.8, but with two key differences: H_2 detection tape (Nitto DX-2106H, Japan) was affixed to the inner wall of the H_2 production device (described in Section S1.5), and natural light was utilized instead of a 300 W Xe lamp (Perfect Light PLS-SXE300+, China).

S1.10. Electronic energy band structure test of $SrTiO_3$:Al

The band gap of $SrTiO_3$:Al was estimated on the basis of the Tauc Equation (3):

$$\mathrm{F(R)}h\nu = \mathrm{A}(h\nu - E_g)^{\frac{n}{2}} \quad (3)$$

in which h, v, A, and E_g represents Planck constant, light frequency, proportionality constant and band gap, respectively, while n depends on the nature of transition in a semiconductor. The values of E_g were determined from the plot of $(\mathrm{F}(R)h\nu)^{2/n}$ against $h\nu$ and corresponded to the intercept of the extrapolated linear portion of the plot near the band edge with the $h\nu$ axis. $SrTiO_3$:Al samples were treated as the semiconductors with allowed direct transition. The values of E_g were thus determined from the plot of $(\mathrm{F}(R)h\nu)^2$ against $h\nu$ (Figure S14b).

The Mott–Schottky (MS) analysis was performed with an Electrochemical workstation (Shanghai Chenhua Instrument Co. CHI760D, China) to characterize the flat band potential of $SrTiO_3$:Al to obtain the conduction band position. In the test, a 0.5 M Na_2SO_4 solution was used as the electrolyte, a photoelectrode was used as the working electrode, a Pt sheet was used as the counter electrode, and an Ag/AgCl (saturated KCl) was used as the reference electrode. The potential versus Ag/AgCl was converted to reversible hydrogen electrode (RHE) using the Equation (4):

$$E_{(\text{versus RHE})} = E_{(\text{versus Ag/AgCl})} + E^{0}_{Ag/AgCl} + 0.0591 \times \text{pH} \quad (4)$$

where $E^{0}_{Ag/AgCl}$= 0.197 versus RHE at 298 K.

S1.11. Detection of $\bullet O_2^-$

The tests were conducted in the presence of light from a Xe lamp (Perfect Light PLS-SXE300+, China). Specifically, 5 mL of methanol was added to NLS-20 in a 50 mL H_2-producing flask followed by an Ar purge for 3 min and then injected with 50 μL of DMPO. Before and after illumination for 10 min, the mixtures were characterized by a Bruker EMX type spectrometer at room temperature and its EPR spectrum was collected.

S1.12. Detection of H_2O_2

The amount of H_2O_2 was analyzed by iodometry.[4] 3 ml of NLS-20 aqueous solution after H_2 production was diluted 20-fold and filtrated with a 0.45 μm to remove the photocatalyst. 1 mL of 0.1 mol L^{-1} $C_8H_5KO_4$ aqueous solution and 1 mL of 0.4 mol L^{-1} KI aqueous solution were added to obtained solution, and kept for 30 min. The amount of I_3^- was determined by means of UV–vis spectroscopy on the basis of the absorbance at 350 nm.

S2. Supporting Tables

Table S1. Specific surface areas and pore volumes of NFC, NL, and NLS-20.

Sample	BET specific surface area (m^2 g^{-1})	Pore volume (single point of pores less than 283.89 nm at P/P_0 =0.9932) (cm^3 g^{-1})
NFC	3.65	0.0202
NL	1.64	0.0047
NLS-20	1.51	0.0045

Table S2. Comparison of water sorption properties of some reported state-of-the-art AWH materials.

Material	Moisture uptake (g_{H_2O} $g_{sorbent}^{-1}$)	Sorption saturation time (min)	Forms and mass of samples	Sample Placement	Testing condition	Ref.
NLS-20	**4.25**	**1440**	Gel **block (9.6 cm^2)**	**-**	**90% RH, 25°C** [a)]	**This work**
MOF-801-hydrazine-0.25	0.292	30	Powders (0.3 g)	NF (5.0×5.0×0.3 cm)	30% RH, 25°C [b)]	5
NBHA	2.36	180	Gel blocks	-	95% RH, 25°C [a)]	6
POG	6.12 [f)]	1440	Gel blocks	-	90% RH, 25°C [a)]	7
LiCl@rGO-SA	2.6	480	Gel block	-	60% RH, 30°C [c)]	8
SHPFs	1.53	~ 240	Gel films (d=0.7 cm)	-	60% RH, [d)]	9
LCP	0.97	~ 600	Gel block (2 g)	LiCl concentrations c 0.4 g g^{-1}	30% RH, 25°C [a)]	10
PDMAPS-LiCl	0.62	120	Gel block	-	30% RH, 25°C [d)]	11
PCLG	1.5 [g)]	~ 250	Gel block	-	30% RH, 30°C [a)]	12
LiCl@HGAFs	0.66	~ 300	Gel block	-	30% RH, [g)]	13
PAMPS-CNT-LiCl	6	600	milligram-scal	-	90% RH, 30°C [d)]	14
HEMHs	2.36	240	Gel films (9×9×2 mm)	-	70% RH, 25°C [a)]	15
SA/CNTs/MC	1.2	720	Gel films	-	70% RH, 20°C [d)]	16
CNF/LiCl-1.5	1.59	720	Gel block	-	95% RH, 25°C [e)]	17
PAMPS-CNT-LiCl	5.45	600	Gel block	-	90% RH, 25°C [d)]	14

[a)] constant temperature and humidity chamber; [b)] Natural surroundings; [c)] thermogravimetric analyzer, equipped with a moisture humidity generator; [d)] dynamic vapor sorption (DVS); [e)] Saturated solutions of KNO_3, [f)] kg m^{-2}, [g)] g cm^{-3}.

Table S3. Comparison of properties of H_2 production from air without intermediate energy supply of some reported state-of-the-art materials.

Material	System Forms and mass	Catalyst components	Atmospheric water sorption Performance	Saturation time	Testing condition	H_2 production Performance	Material supply	Energy supply	Ref
NLS-20	**Block, 9.6 cm^2**	**$SrTiO_3$:Al, 20 mg**	**4.26 g_{H_2O} g_{NLS-20}^{-1}**	**24 h**	**90% RH, 25°C**	**65.45 μmol h^{-1}**	**H_2O**	**Simulated light**	**This work**
CW550/Pt-CN	Block, 4 cm^2	Pt-CN, 50 mg	0.56 g_{H_2O} $g_{CW550/Pt-CN}^{-1}$	-	70%RH	15.99 μmol h^{-1}	H_2O	Simulated light	[18]
Pt-Py-HMPA	Powder, 5 mg	Pt-Py-HMPA, 5 mg	-	-	65%-50% RH, 20-28°C	0.53 μmol h^{-1}	25 mL of H_2O containing 0.1 M ascorbic acid	Simulated light	[19]
$CaCl_2$-PAAm-Pt-TiO_2/PTFE	Block, 28.27 cm2	Pt-TiO_2, 70 mg	~0.52 g_{H_2O} $g_{CaCl_2-PAAm}^{-1}$	~8 h	75% RH	29.78 μmol h^{-1}	H_2O with polyethylene glycol 2000	Simulated light	[20]

Table S4. Comparison of properties of H_2 production from air with intermediate energy supply of some reported state-of-the-art materials.

System				Atmospheric water sorption			H_2 production			Ref
Cathode	Anode	Reference electrode	Electrolyte	Performance	Testing condition	Performance	Photocurrent	Energy supply	Technology	
Pt mesh (4 cm^2)	Ni Foam (4 cm^2)	-	melamine sponge/KOH (7.84 cm^2)	0.75 g_{H_2O} g_{KOH}^{-1}	60% RH	-	574 mA cm^{-2}	Constant current (4.0V)	Electrocatalytic	21
				0.5 g_{H_2O} g_{KOH}^{-1}	15% RH	-	177 mA cm^{-2}	Constant current (3.0V)		
Pt mesh (4 cm^2)	Ni Foam (4 cm^2)	-	melamine sponge/KOH (7.84 cm^2)	-	20-40% RH, 20-40°C	8.3 mmol h^{-1}	400 mA	Solar panel (6.0 V, 400 mA)	Photovoltaic-electrocatalytic	21
Pt sheet (4 cm^2)	$BaTiO_3$@$BiVO_4$ (1 cm^2)	Ag/AgCl	Co hydrogel (0.5 mL)	-	70.0% RH	-	0.4 mA cm^2	Polysilicon solar cell (1.15 V under 10 mW cm^{-2} LED illumination）		22
BTO@MoS_2 on carbon cloth (1 cm^2)	BTO@MoS_2 on carbon cloth (1 cm^2)	-	Co hydrogel (200 mg)	2 g_{H_2O} $g_{Co\ hydrogel}^{-1}$	80%RH	0.178 mmol h^{-1}	12.5 mA cm^{-2}	Polysilicon solar cell (4.8 V, 15.6 mA under 10 mW cm^{-2} LED illumination)		23
FeOOH/Cu_2O	FeOOH/$BiVO_4$	-	Co Super-hygroscopic hydrogel	-	95%RH	30 μmol h^{-1}	2 mA cm^{-2}	Polysilicon solar cell (0 V under 100 mW cm^{-2})		24
FeOOH/Cu_2O	FeOOH/$BiVO_4$	-	Co Super-hygroscopic hydrogel	-	95%RH		0.75 mA cm^{-2}	100 mW cm^{-2} illumination	Photo-electrocatalysis	24
Pt sheet	Cu_2O@BTO (100 mg) on fluorine doped tin oxide	Ag/AgCl	Co hydrogel (150.2 mg, 18 cm^2)	-	70.0% RH	-	224.3 μA cm^{-2}	Constant applied voltage of 0 V versus reversible hydrogen electrode (RHE) under 10 mW cm^{-2} LED illumination		25

Table S5. Comparison of H_2 production performance of $SrTiO_3$:Al in the NLS-20 System and in a suspension environment.

Sample	$SrTiO_3$:Al Co-catalyst	Mass	Material supply	Energy supply	Background pressure	H_2 production rate
NLS-20 (Block, 9.6 cm^2)	Rh/CrO_x	20 mg	Atmospheric water (~4.5 g)	Simulated light (1.4 sun)	Atmospheric pressure	65.45 (μmol h^{-1})
$SrTiO_3$:Al (suspension)	Rh/CrO_x	20 mg	Purified liquid water (50 g)	Simulated light (1.4 sun)	Atmospheric pressure	82.84 (μmol h^{-1})

Table S6. Amount of H_2O_2 in aqueous solution before and after NLS-20 H_2 production.

Sample	Absorbance (a.u)	Concentration of H_2O_2 (μmol L^{-1})		Amount of H_2O_2 (μmol)
		Sample tested	Entire system	
NLS-20 after H_2 production	0.22374	25.52	510.41	3.36
Moisture-absorbed NLS-20	0.06677	12.68	12.68	0.05

S3. Supporting Figures

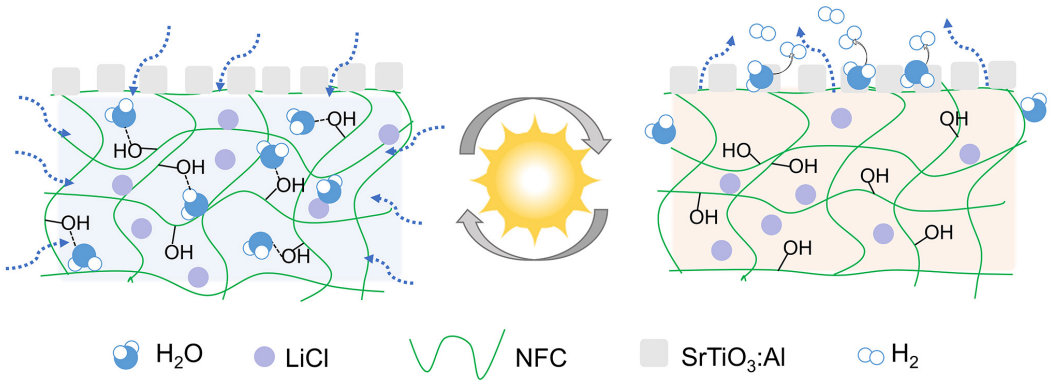

Figure S1. Schematic illustration of the process of H_2 production from air by NLS-*x*, including moisture absorption (left) and solar-driven water desorption and H_2 production (right).

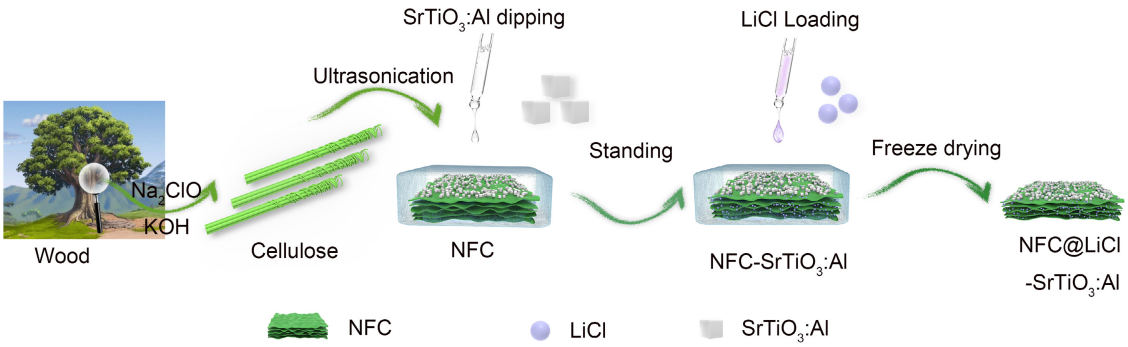

Figure S2. Schematic illustration of the experimental fabrication process of NLS-*x*.

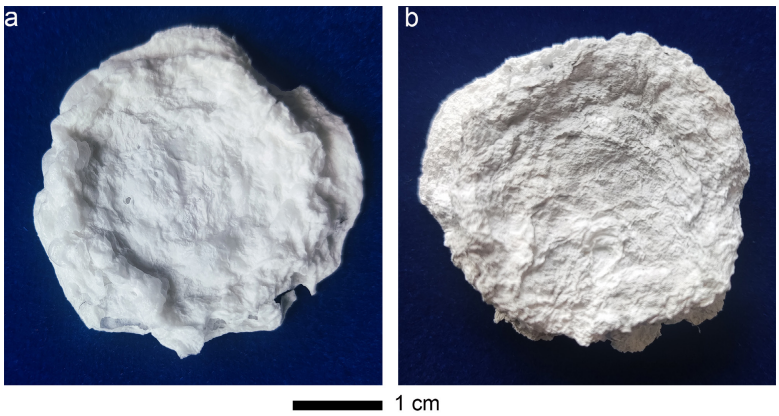

Figure S3. Digital images of (a) NL and (b) NLS-20. Scale bar: (a-b) 1 cm.

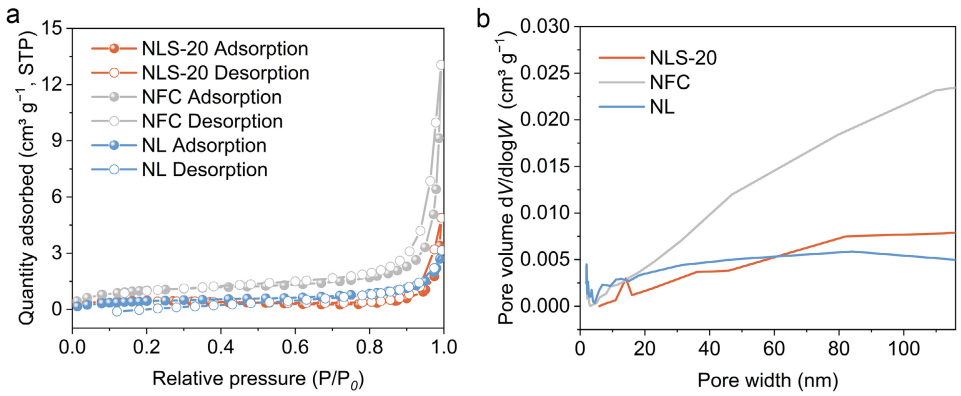

Figure S4. (a) N_2 adsorption-desorption isotherms, and derived (b) pore-size distribution curves of NLS-20, NFC, and NL.

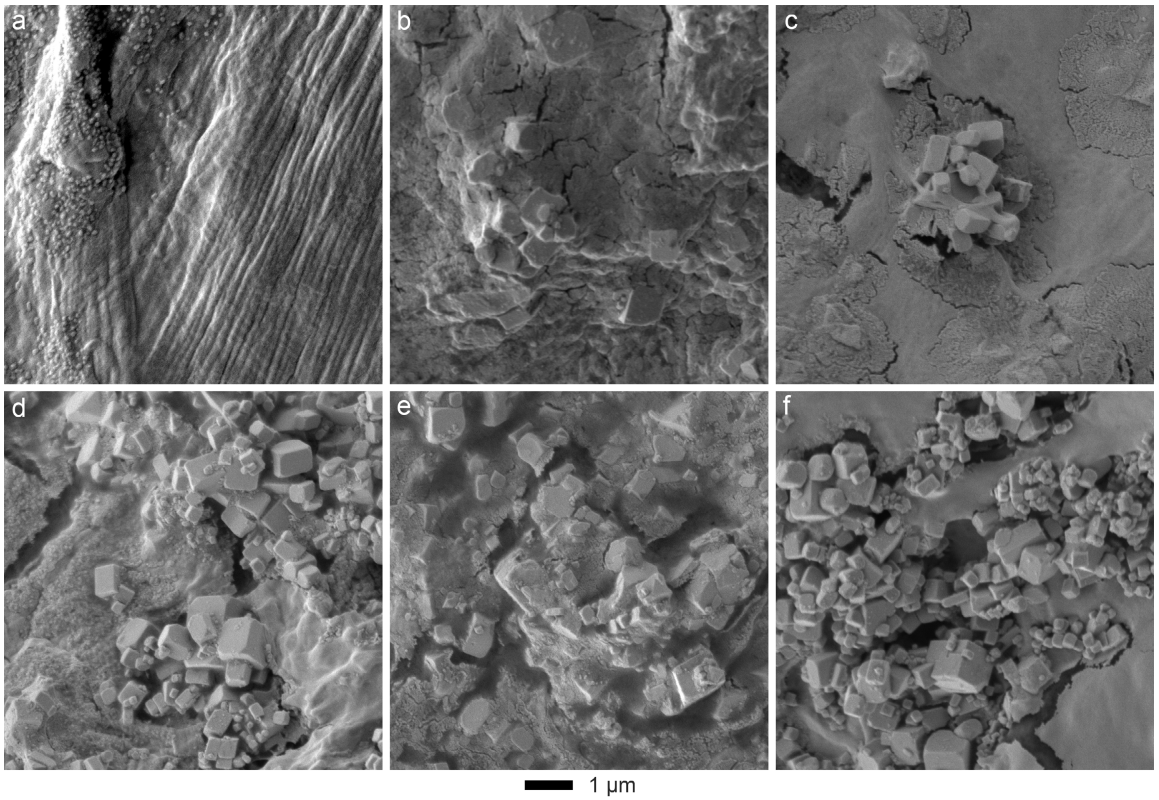

Figure S5. SEM images of (a) NL, (b) NLS-5, (c) NLS-10, (d) NLS-20, (e) NLS-40, and (f) NLS-80. Scale bar: (a-f) 1 μm.

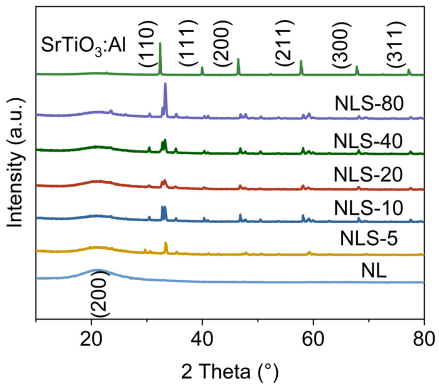

Figure S6. XRD patterns of prepared NL, NLS-*x*, and $SrTiO_3$:Al.

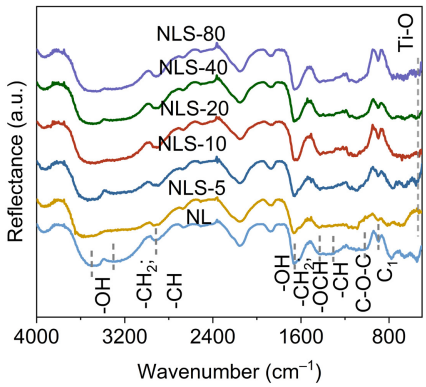

Figure S7. FTIR spectra of prepared NL, NLS-*x*, and $SrTiO_3$:Al.

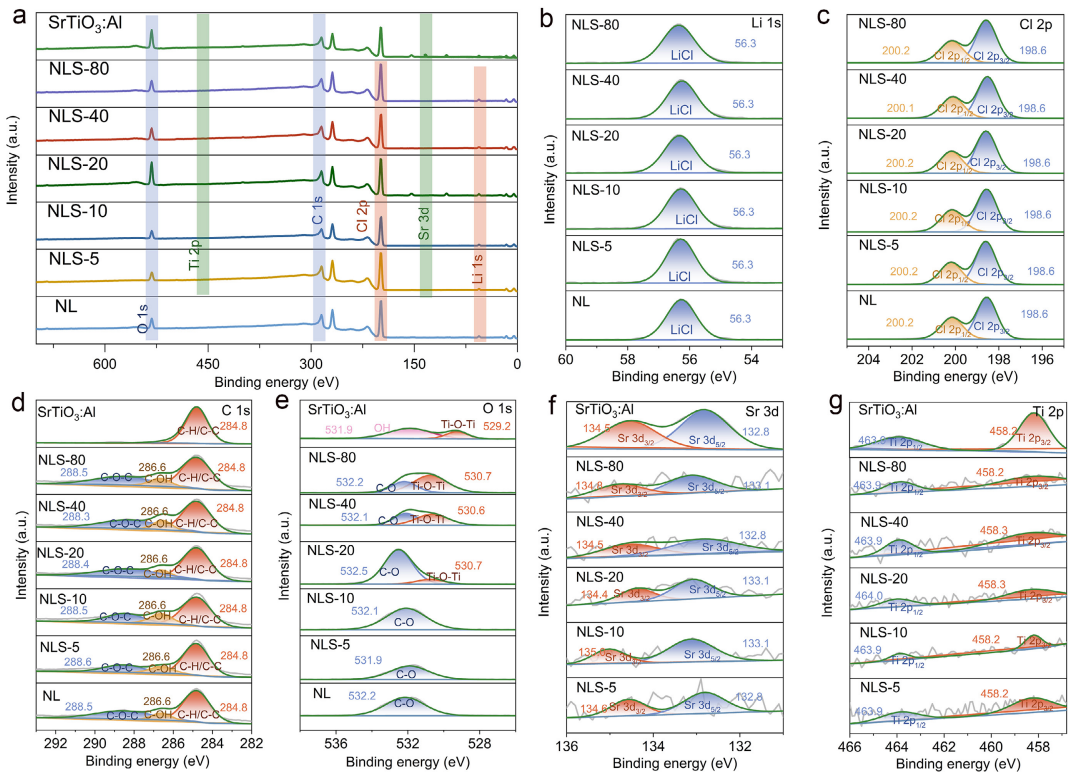

Figure S8. (a) XPS survey spectrum of prepared NL, NLS-*x*, and $SrTiO_3$:Al and high-resolution XPS spectra of (b) Li 1s, (c) Cl 2p, (d) C 1s, (e) O 1s, (f) Sr 3d, and (g) Ti 2p in the prepared samples.

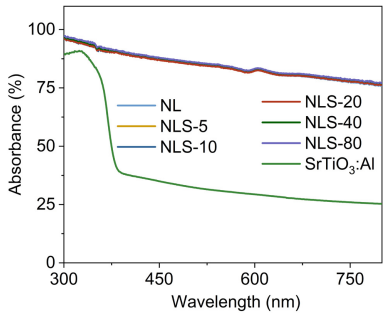

Figure S9. UV–vis absorption spectra of prepared NL, NLS-*x*, and $SrTiO_3$:Al.

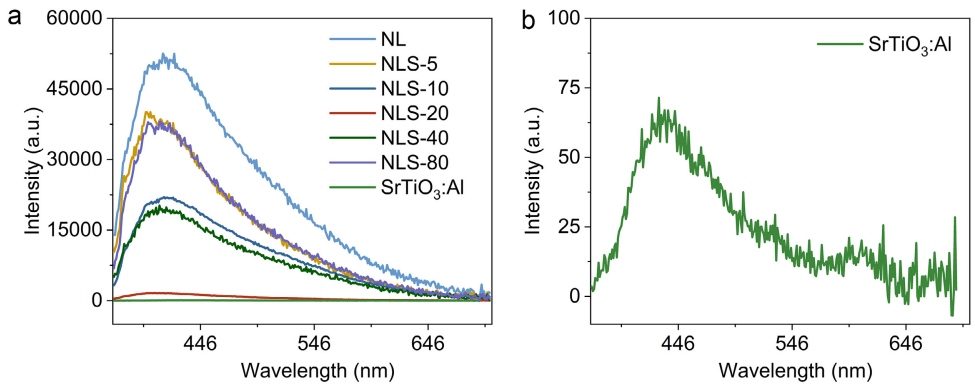

Figure S10. (a) The PL spectra of prepared NLS-*x* and $SrTiO_3$:Al. (b) An amplification PL spectrum of $SrTiO_3$:Al in Figure S10a.

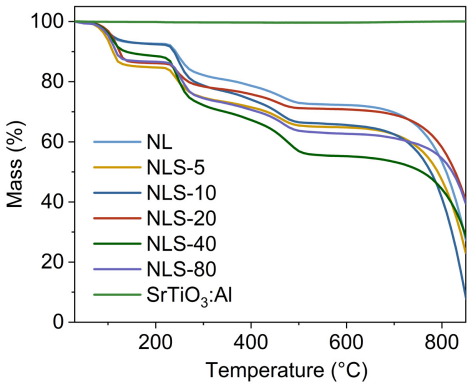

Figure S11. TGA curves of prepared NL, NLS-*x*, and $SrTiO_3$:Al.

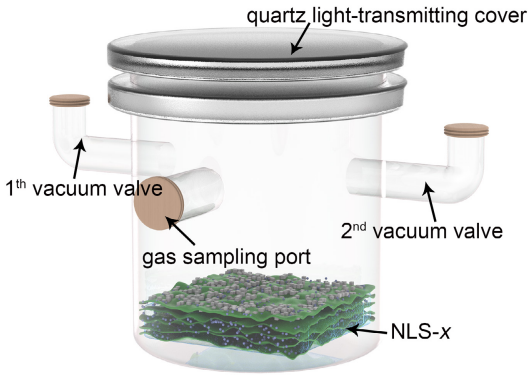

Figure S12. The design of device for photocatalytic atmospheric water splitting for H_2 production.

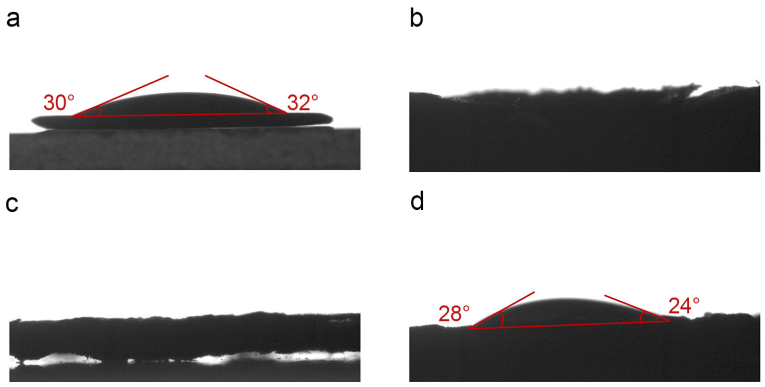

Figure S13. Water contact angles of (a) $SrTiO_3$:Al, (b) NFC, (c) NL, and (d) NLS-20. The droplet size and tube diameter used during the contact angles measurement were 6 μL and 2.5 mm, respectively.

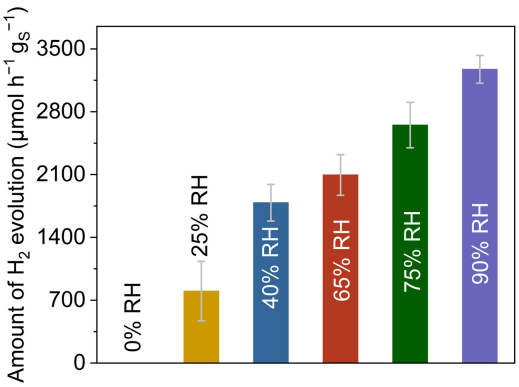

Figure S14. The H_2 production activity of NLS-20 after moisture sorption in different RHs.

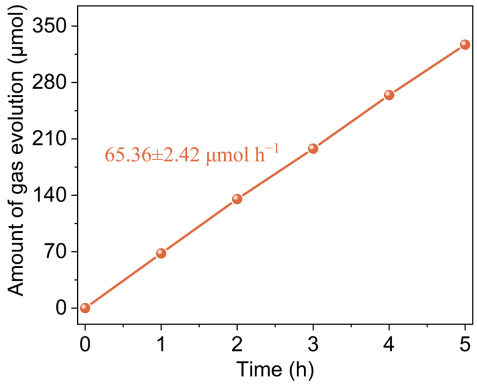

Figure S15. Time-courses of H_2 production over NLS-20 under Xe-lamp irradiation.

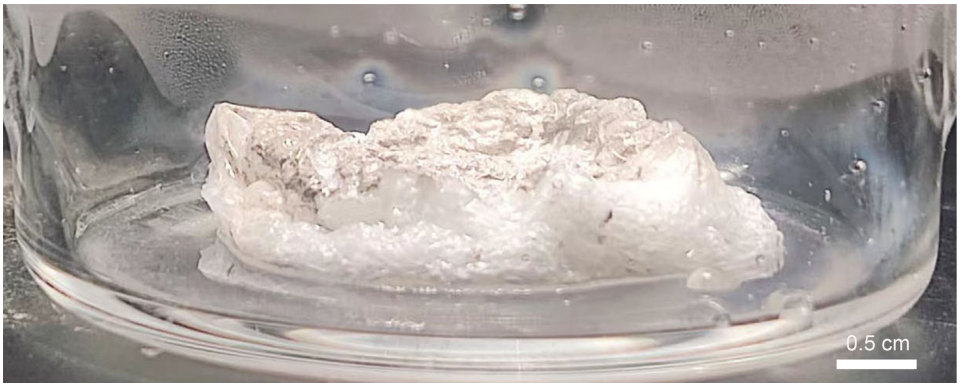

Figure S16. Physical diagram of NLS-20, which saturated with hygroscopicity at 90% RH undergoing solar-powered atmospheric water desorption-H_2 production. Scale bar: 0.5 cm.

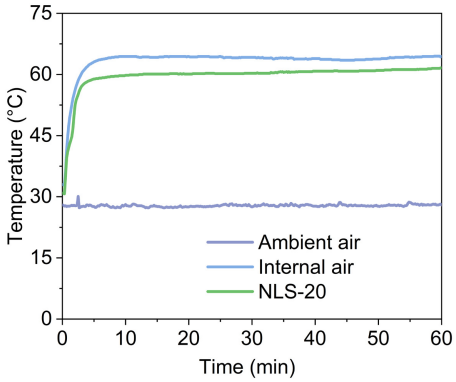

Figure S17. The real-time temperature evolution of NLS-20, internal air, and ambient air during solar-powered atmospheric water desorption-H_2 production.

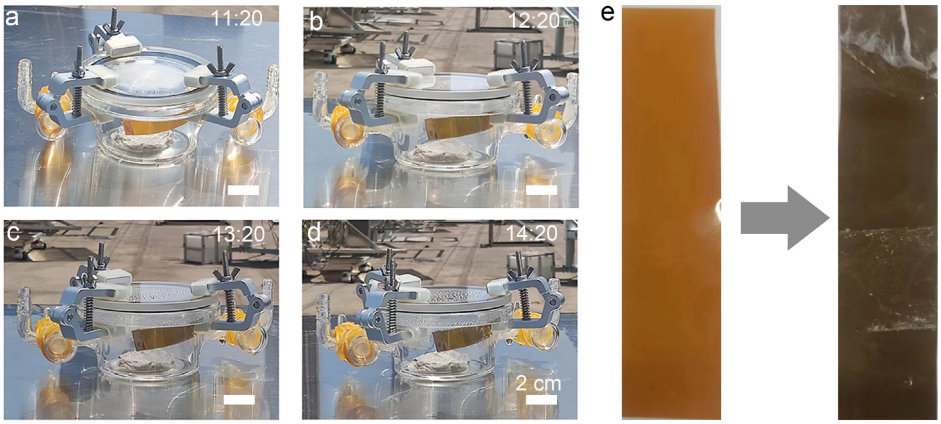

Figure S18. (a-d) Digital photographs depict the process of in-situ H_2 production from air using NLS-20 over time. (e) Photographs of the H_2 detection tape, shown before (left) and after (right) the outdoor H_2 production reaction. Scale bar: (a-d) 2 cm.

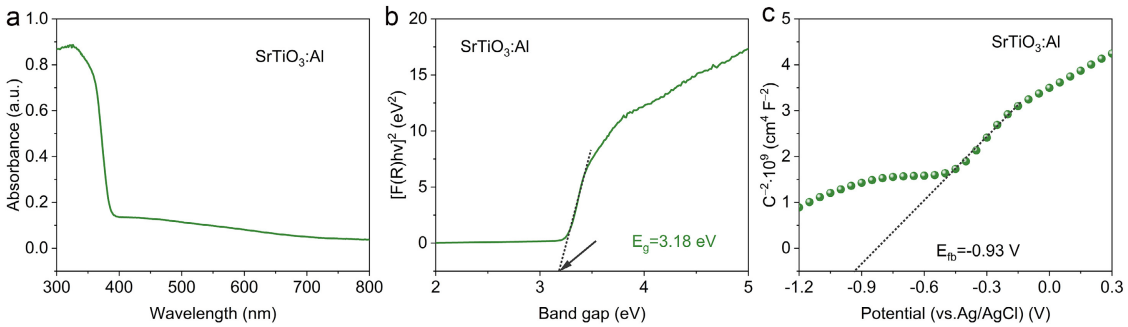

Figure S19. (a) UV–vis absorption spectrum of $SrTiO_3$:Al. (b) Tauc plot of $SrTiO_3$:Al using $[F(R)hv]^2$ (Kubelka-Munk function) as a function of photon energy. (c) Mott-Schottky plot of $SrTiO_3$:Al.

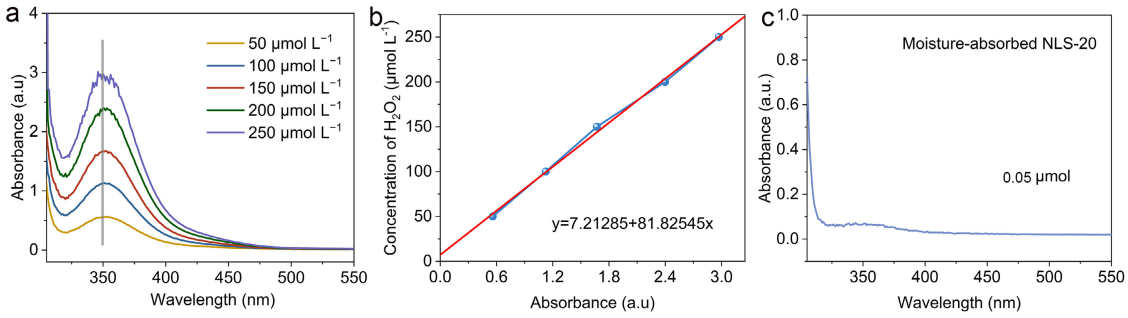

Figure S20. (a) UV–vis absorption spectra of H_2O_2 at different concentrations. (b) Standard curve of H_2O_2 concentration over UV–vis absorbance. (c) UV–vis spectrum of moisture-absorbed NLS-20 aqueous solution.

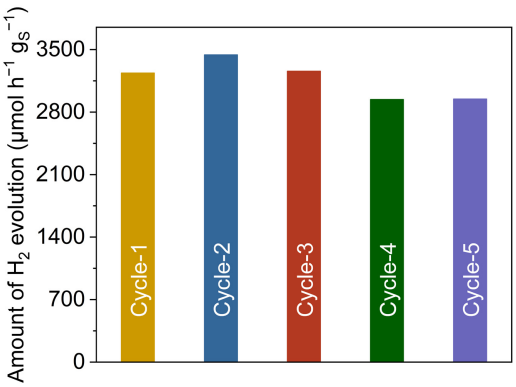

Figure S21. Cycling stability assessment of photocatalytic atmospheric water splitting of NLS-20 for H_2 production performance.

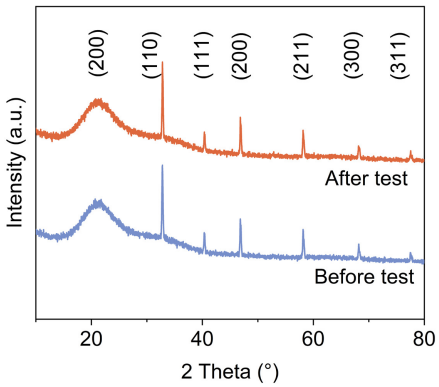

Figure S22. XRD patterns of NLS-20 before and after atmospheric water absorption-desorption-H_2 production.

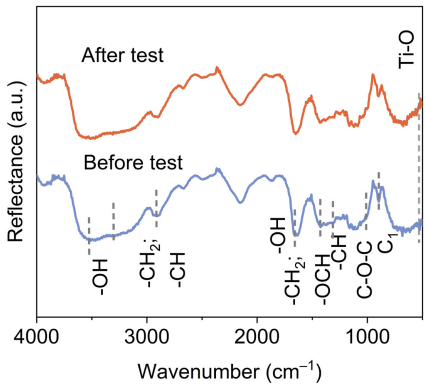

Figure S23. FTIR spectra of NLS-20 before and after atmospheric water absorption-desorption-H_2 production.

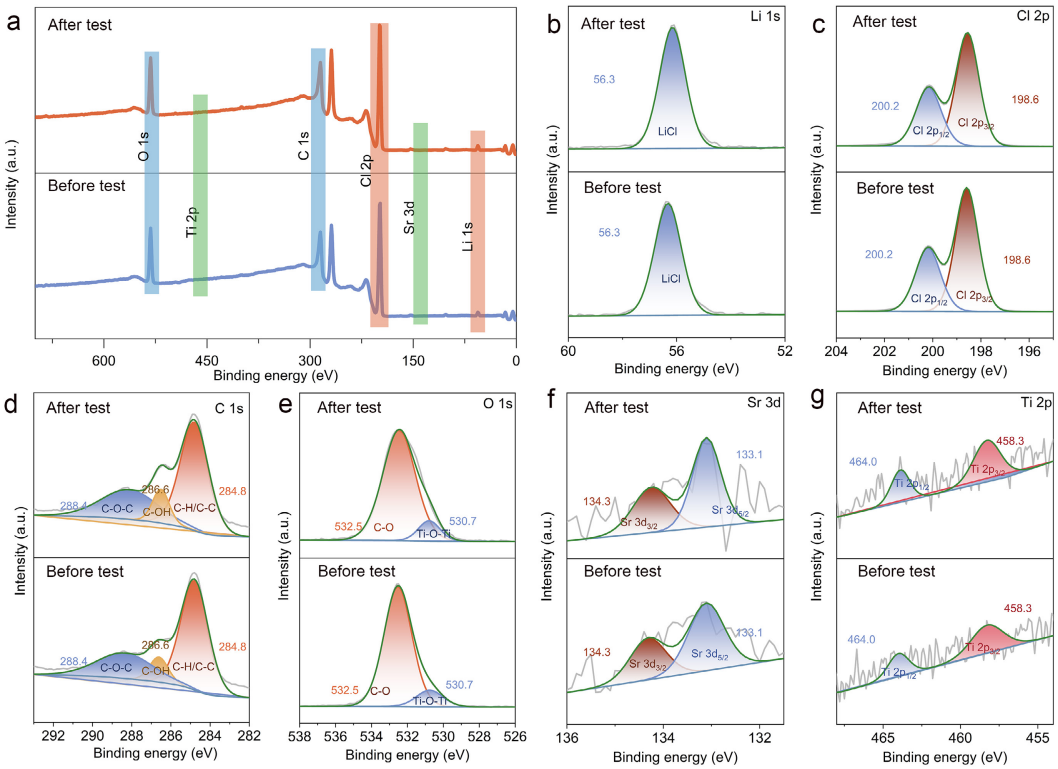

Figure S24. (a) XPS survey spectrum of NLS-20 before and after atmospheric water absorption-desorption-H_2 production and high-resolution XPS spectra of (b) Li 1s, (c) Cl 2p, (d) C 1s, (e) O 1s, (f) Sr 3d, and (g) Ti 2p.

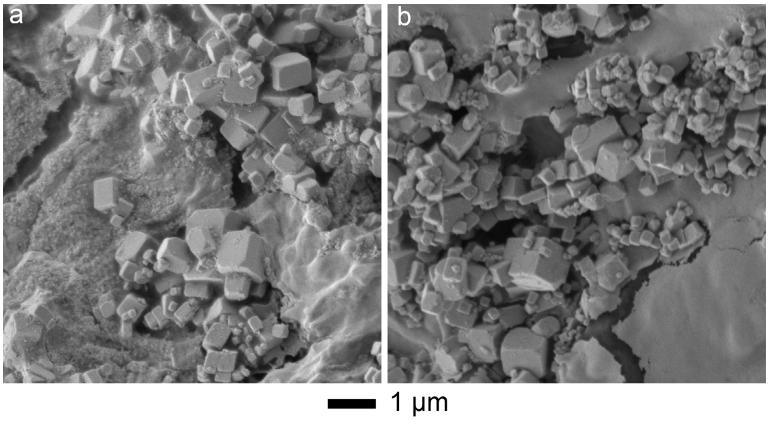

Figure S25. SEM images of NLS-20 (a) before and (b) after atmospheric water absorption-desorption-H_2 production. Scale bar: (a-b) 1μm.

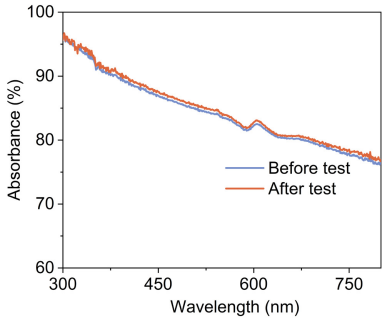

Figure S26. UV–vis spectra of NLS-20 before and after atmospheric water absorption-desorption-H_2 production.

S4. Supporting References

1. T. Takata, J. Jiang, Y. Sakata, M. Nakabayashi, N. Shibata, V. Nandal, K. Seki, T. Hisatomi and K. Domen, *Nature*, 2020, **581**, 411-414.
2. M. Dai, F. Zhao, J. Fan, Q. Li, Y. Yang, Z. Fan, S. Ling, H. Yu, S. Liu, J. Li, W. Chen and G. Yu, *Adv. Mater.*, 2022, **34**, 2200865.
3. M. Wang, T. Sun, D. Wan, M. Dai, S. Ling, J. Wang, Y. Liu, Y. Fang, S. Xu, J. Yeo, H. Yu, S. Liu, Q. Wang, J. Li, Y. Yang, Z. Fan and W. Chen, *Nano Energy*, 2021, **80**, 105569.
4. C. Feng, L. Tang, Y. Deng, J. Wang, J. Luo, Y. Liu, X. Ouyang, H. Yang, J. Yu and J. Wang, *Adv. Funct. Mater.*, 2020, **30**, 2001922.
5. X. Yan, F. Xue, C. Zhang, H. Peng, J. Huang, F. Liu, K. Lu, R. Wang, J. Shi, N. Li, W. Chen and M. Liu, *EcoMat*, 2024, **6**, e12473.
6. M. Wang, T. Sun, D. Wan, M. Dai, S. Ling, J. Wang, Y. Liu, Y. Fang, S. Xu and J. Yeo, *Nano Energy*, 2021, **80**, 105569.
7. F. Ni, N. Qiu, P. Xiao, C. Zhang, Y. Jian, Y. Liang, W. Xie, L. Yan and T. Chen, *Angew. Chem. Int. Ed.*, 2020, **59**, 19237-19246.
8. J. Xu, T. Li, T. Yan, S. Wu, M. Wu, J. Chao, X. Huo, P. Wang and R. Wang, *Energy Environ. Sci.*, 2021, **14**, 5979-5994.
9. Y. Guo, W. Guan, C. Lei, H. Lu, W. Shi and G. Yu, *Nat. Commun.*, 2022, **13**, 2761.
10. T. Lyu, Z. Wang, R. Liu, K. Chen, H. Liu and Y. Tian, *ACS Appl. Mater. Interfaces*, 2022, **14**, 32433-32443.
11. C. Lei, Y. Guo, W. Guan, H. Lu, W. Shi and G. Yu, *Angew. Chem. Int. Ed.*, 2022, **61**, e202200271.
12. J. Wang, C. Deng, G. Zhong, W. Ying, C. Li, S. Wang, Y. Liu, R. Wang and H. Zhang, *Cell Rep. Phys. Sci.*, 2022, **3**, 100954.
13. Y. Hou, Z. Sheng, C. Fu, J. Kong and X. Zhang, *Nat. Commun.*, 2022, **13**, 1227.
14. H. Shan, P. Poredoš, Z. Ye, H. Qu, Y. Zhang, M. Zhou, R. Wang and S. C. Tan, *Adv. Mater.*, 2023, **35**, 2302038.
15. J. Sun, F. Ni, J. Gu, M. Si, D. Liu, C. Zhang, X. Shui, P. Xiao and T. Chen, *Adv. Mater.*, 2024, **36**, 2314175.
16. X. Zhang, H. Qu, X. Li, L. Zhang, Y. Zhang, J. Yang, M. Zhou, L. Suresh, S. Liu and S. C. Tan, *Adv. Mater.*, 2310219.
17. P. Zhu, Z. Yu, H. Sun, D. Zheng, Y. Zheng, Y. Qian, Y. Wei, J. Lee, S. Srebnik, W. Chen, G. Chen and F. Jiang, *Adv. Mater.*, 2024, **36**, 2306653.
18. L. He, X. Zeng, H. Chen, L. Zhao, Z. Huang, D. Wang, X. He, W. Fang, X. Du and W. Li, *Adv. Funct. Mater.*, 2024, **34**, 2313058.
19. Y. Liu, W.-K. Han, W. Chi, J.-X. Fu, Y. Mao, X. Yan, J.-X. Shao, Y. Jiang and Z.-G. Gu, *Appl. Catal. B*, 2023, **338**, 123074.
20. L. Huang, P. Liu, C. Qin, C. Gui, X. Zhang, T. Ren, Y. Ge, Y. Yu, Z. Liu and L. Chen, *Nano Energy*, 2024, **128**, 109879.
21. J. Guo, Y. Zhang, A. Zavabeti, K. Chen, Y. Guo, G. Hu, X. Fan and G. K. Li, *Nat. Commun.*, 2022, **13**, 5046.
22. L. Yang, D. K. Nandakumar, L. Miao, L. Suresh, D. Zhang, T. Xiong, J. V. Vaghasiya, K. C. Kwon and S. Ching Tan, *Joule*, 2020, **4**, 176-188.

23. L. Yang, L. Loh, D. K. Nandakumar, W. Lu, M. Gao, X. L. C. Wee, K. Zeng, M. Bosman and S. C. Tan, *Adv. Mater.*, 2020, **32**, 2000971.
24. L. Yang, D. K. Nandakumar, L. Suresh, S. Zhang, Y. Zhang, L. Zhang, J. Wang, J. W. Ager and S. C. Tan, *ACS Nano*, 2021, **15**, 19119-19127.
25. L. Yang, S. K. Ravi, D. K. Nandakumar, F. I. Alzakia, W. Lu, Y. Zhang, J. Yang, Q. Zhang, X. Zhang and S. C. Tan, *Adv. Mater.*, 2019, **31**, 1902963.